Dalton Transactions

Spin reorientation and magnetic frustration in $Fe_{32+\delta}Ge_{35-x}Si_x$ with a kagome lattice broken by crystallographic intergrowth

Journal:	*Dalton Transactions*
Manuscript ID	DT-ART-03-2025-000654.R1
Article Type:	Paper
Date Submitted by the Author:	14-Apr-2025

Complete List of Authors:	Khalaniya, Roman; Lomonosov Moscow State University, Department of Chemistry Verchenko, Valeriy; Lomonosov Moscow State University, Department of Chemistry Mironov, Andrey; Lomonosov Moscow State University, Department of Chemistry Samarin, Alexander; Prokhorov General Physics Institute RAS Bogach, Alexey; Institute of General Physics named after A P Prokhorov Russian Academy of Sciences; Lomonosov Moscow State University, Department of Chemistry Kulchu, Aleksandr; Lomonosov Moscow State University, Department of Chemistry Polevik, Alexey; Lomonosov Moscow State University, Department of Chemistry Zheng, Wei; University at Albany, Chemistry Dikarev, Evgeny; University at Albany, Chemistry Stern, Raivo; NICPB, Chemical Physics Shevelkov, Andrei; Lomonosov Moscow State University, Department of Chemistry

ARTICLE

Spin reorientation and magnetic frustration in $Fe_{32+\delta}Ge_{35-x}Si_x$ with a kagome lattice broken by crystallographic intergrowth†

Received 00th January 20xx,
Accepted 00th January 20xx

DOI: 10.1039/x0xx00000x

Roman A. Khalaniya,[a] Valeriy Yu. Verchenko,[a] Andrei V. Mironov,[a] Alexander N. Samarin,[b] Alexey V. Bogach,[ab] Aleksandr N. Kulchu,[a] Alexey O. Polevik,[a] Zheng Wei,[c] Evgeny V. Dikarev,[c] Raivo Stern,[d] and Andrei V. Shevelkov [a]

$Fe_{32+\delta}Ge_{35-x}Si_x$ was synthesized using solid-state and chemical vapor transport reactions both in powder and single crystalline forms. Single crystal and high-resolution powder X-ray diffraction experiments revealed $Fe_{32+\delta}Ge_{35-x}Si_x$ to be a third member of the $Fe_{32+\delta}Ge_{35-x}E_x$ (E = *p*-element) family of ternary compounds alongside $Fe_{32+\delta}Ge_{33}As_2$ and $Fe_{32+\delta}Ge_{35-x}P_x$. $Fe_{32+\delta}Ge_{35-x}Si_x$ features a two-dimensional intergrowth structure of two parent structure types: $MgFe_6Ge_6$ and Co_2Al_5. Similarly to the other members, the stabilisation of the intergrowth structure in $Fe_{32+\delta}Ge_{35-x}Si_x$ occurs as a result of the *p*-element substitution in the $MgFe_6Ge_6$-type block. The intergrowth breaks the kagome net of $MgFe_6Ge_6$ into individual hexagrams, while providing additional layers of geometrically frustrated atomic arrangements. Magnetic measurements showed antiferromagnetic ordering at T_N ~ 150-160 K and spin reorientation below 80-90 K owing to the competition between magnetic interactions in the frustrated magnetic lattice of $Fe_{32+\delta}Ge_{35-x}Si_x$.

.

Introduction

Compounds with the kagome (or kagomé)[1] lattice have long been attracting attention as emergent materials for spintronic and quantum computing applications owing to the unique magnetic and electron transport properties.[2-4] Due to the underlying geometric frustration, kagome compounds can display various types of unusual magnetic behaviour, including skyrmion ordering[5] and spin-liquid phases.[6] In the kagome metals, the magnetic ordering is intertwined with the electron transport giving rise to large anomalous and topological Hall effects.[7,8] Recent studies of the kagome metals also showed that the geometry of the kagome lattice can lead to various non-trivial features not only in the real space but in the reciprocal space as well. Kagome metals feature Weyl semimetals, such as $Co_3Sn_2S_2$,[9] Mn_3Sn,[10] and Mn_3Ge,[10] and unconventional superconductors AV_3Sb_5 (A = K, Cs, Rb) with time reversal symmetry breaking.[11]

Various similar lattices that share frustrated trigonal arrangements of atoms were also observed in other inorganic compounds, including breathing kagome,[12,13] hyperkagome,[14] kagome staircase,[15] square kagome,[16] depleated kagome,[17] and shurikagome[18] lattices. Such derivative lattices can preserve some features of the kagome lattice including magnetic frustration and nontrivial topology of the electronic structure.[12–18] Previously, we have presented another way to modify the kagome lattice, which is realized in two ternary intermetallic compounds – $Fe_{32+\delta}Ge_{33}As_2$ and $Fe_{32+\delta}Ge_{35-x}P_x$ forming as a result of the *p*-element substitution.[19-21] These compounds feature rare two-dimensional intergrowth structures with columns of the $MgFe_6Ge_6$ structure type[22] and Co_2Al_5 structure type[23] alternating in the same plane. The intergrowth breaks the kagome lattice inherited from $MgFe_6Ge_6$ into separate hexagrams, which are arranged in a triangular lattice. Despite lattice modifications, the geometric frustration is preserved, as the compounds feature relatively low Neel temperatures of 125 K, while showing Weiss temperatures θ_W below −400 K.[19,20] Below the transition temperatures, the underlying frustration causes the compounds to exhibit complex non-colinear magnetic structures, which change with the temperature due to spin reorientation.[21]

Herein, we report on the third member of this family of compounds, $Fe_{32+\delta}Ge_{35-x}Si_x$. A possible existence of the Si-based member of this family was previously mentioned in the literature; however, no specific details were provided.[24] In this paper, we present its synthesis as both polycrystalline powders

[a] Department of Chemistry, Lomonosov Moscow State University, 119991 Moscow, Russia. E-mail: khalaniya@inorg.chem.msu.ru
[b] Prokhorov General Physics Institute of the Russian Academy of Sciences, 119991 Moscow, Russia
[c] Department of Chemistry, University at Albany, Albany, 12222 New York, United States
[d] National Institute of Chemical Physics and Biophysics, 12618 Tallinn, Estonia

† Electronic Supplementary Information (ESI) available: additional crystallographic and magnetisation data. CCDC 2431926–2431930. See DOI: 10.1039/x0xx00000x

and single crystals, the crystal structure obtained from high resolution X-ray diffraction on both powder and single crystal samples, and magnetic properties, including magnetic anisotropy. We discuss them in comparison with those of $Fe_{32+\delta}Ge_{33}As_2$ and $Fe_{32+\delta}Ge_{35-x}P_x$, as well as other related phases, and highlight the peculiarities that make $Fe_{32+\delta}Ge_{35-x}Si_x$ unique within this family of compounds.

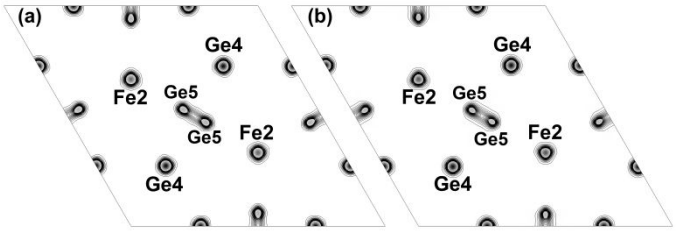

Fig. 1 Experimental electronic density maps at $z = 0$ for the $Fe_{32.6}Ge_{33}Si_2$ single crystal at 100 K (a) and the $Fe_{32.8}Ge_{30}Si_5$ single crystal at 293 K (b) obtained using the maximum entropy method implemented in the Dysnomia program.[26] The maps are visualized using the VESTA software.[27]

Experimental

Synthesis and characterisation

Polycrystalline samples of $Fe_{32+\delta}Ge_{35-x}Si_x$ were obtained by a solid-state reaction of Fe_5Si_3, FeGe, and $FeGe_2$ at 800°C. Elemental ratios of starting reagents corresponded to $Fe_{32.7}Ge_{35-x}Si_x$, where x was varied in the range of 2-7.5 with a step in x of 0.5. Fe_5Si_3 and the mixtures of FeGe and $FeGe_2$ were prepared separately from the elements. Powders of high purity Fe, Ge, and Si were used for the synthesis of the compounds. Fe_5Si_3 was prepared by a solid-state reaction at 900°C for the duration of 7 days. The mixtures of FeGe and $FeGe_2$ were obtained by a two-step synthesis with annealing at 1000°C for 2 days followed by a second annealing at 650°C for 7 days of the ground and pressed in pellets samples. To prevent oxidation, all samples were annealed in evacuated and sealed silica tubes.

Such a complicated synthetic route was necessary to surmount the intrinsically low reactivity of Si and also to prevent the formation of the inert $FeGe_{1-x}Si_x$ cubic phase during the synthesis, since our attempts to prepare $Fe_{32+\delta}Ge_{35-x}Si_x$ directly from the elements using conventional techniques were unsuccessful. A solid-state reaction of the elements at 650-800°C for the duration of 7 days results in the formation of cubic $FeGe_{1-x}Si_x$ solid solution, FeGe, $FeGe_2$, and only a small amount of the target phase with some amount of unreacted Si remaining. Annealing of the elements at 1000 °C for two days results in binary iron germanides and recrystallised silicon.

The single crystal growth of $Fe_{32+\delta}Ge_{35-x}Si_x$ was attempted using several different techniques that employ chemical vapor transport reactions. Isothermal reaction of the elemental mixture with a $Fe_{32}Ge_{33}Si_2$ composition with iodine at 650°C yielded several small rod-shaped crystals of the target phase, each measured approximately 0.1-0.2 mm in length after a week of annealing. One of these crystals was used for the structural analysis (*vide infra*).

Attempts to obtain larger single crystals of $Fe_{32+\delta}Ge_{35-x}Si_x$ from the respective stoichiometric mixtures in a temperature gradient yielded only a handful of small crystals or no crystals at all if both evaporation and crystallisation zones were set below 700°C. Other transporting agents were also tested, but did not produce crystals of $Fe_{32+\delta}Ge_{35-x}Si_x$.

Large crystals were obtained at elevated temperatures using a noticeable excess of silicon or employing the surface of the silica tubes as the source of silicon by adding Al chips into the mixture. The following initial compositions were found to be suitable for growing single crystals of $Fe_{32+\delta}Ge_{35-x}Si_x$: $Fe_6Ge_4Al_2$, $Fe_6Ge_4AlSi_2$, $Fe_6Ge_4Al_2Si$, $Fe_6Ge_4Si_2$, and $Fe_6Ge_4Si_3$. The annealing temperatures were also varied, and the temperature gradient of 800-700°C was found out to be an optimal regime for growing single crystals of $Fe_{32+\delta}Ge_{35-x}Si_x$. As a side product of the synthesis, crystals of Ge and $FeGe_{1-x}Si_x$ were always found after annealing. However, they can be sorted out by their distinct appearance. One of the smaller single crystals obtained from the $Fe_6Ge_4AlSi_2$ mixture after a month of annealing was used for the X-ray diffraction analysis, while a larger rod and a twinned lump were used for magnetic studies (*vide infra*).

Phase analysis of the obtained samples was performed by X-ray diffraction using Cu $K\alpha_1$ radiation (Huber G670 diffractometer, $\lambda = 1.54056$ Å). The elemental composition of the single crystals was studied by means of EDX spectroscopy using an electron microscope JSM JEOL 6490LV operated at 30 kV and equipped with an EDX detection system INCA X-Sight. Due to relatively small concentration of the Si atoms in the crystals and high absorption of their characteristic X-ray in the sample, the apparent concentration of Si varies heavily with the tilt of a studied edge of the crystal, while the Fe/Ge ratio remains practically identical. Thus, the EDX analysis gives only a rough estimation of the real elemental composition in our case. The EDX analysis showed that the small single crystal obtained from the $Fe_{32}Ge_{33}Si_2$ mixture at 650°C corresponded to a $Fe_{32.5(3)}Ge_{32.75(10)}Si_{2.3(2)}$ composition, while the small single crystal obtained from the $Fe_6Ge_4AlSi_2$ mixture was shown to have a $Fe_{32.65(14)}Ge_{29.13(7)}Si_{5.87(17)}$ composition. The elemental composition of the larger crystals from the latter sample was determined to be $Fe_{31.96(16)}Ge_{29.08(5)}Si_{5.92(15)}$ for the needle and $Fe_{32.22(10)}Ge_{29.23(8)}Si_{5.77(5)}$ and for the twinned crystal. While being present in the initial mixture for this sample, no traces of Al were found in the crystals.

Crystal structure determination

Single-crystal X-ray diffraction experiments were performed at 100 K using a Bruker D8 VENTURE diffractometer (Mo Kα, λ = 0.71073 Å) for the single crystal obtained from the $Fe_{32}Ge_{33}Si_2$ mixture at 650°C. The single crystal obtained from the $Fe_6Ge_4AlSi_2$ mixture was studied at room temperature using a Nonius CAD-4 diffractometer (Ag Kα, λ = 0.56083 Å). Details of the single crystal diffraction experiments are summarized in Table 1. Atomic parameters for the crystals are given in Table 2.

The most important interatomic distances in comparison with those for $Fe_{32+\delta}Ge_{33}As_2$ and $Fe_{32+\delta}Ge_{35-x}P_x$ are presented in Electronic Supplementary Information (ESI†, Table S1). The crystallographic information files for the single crystals are available from CCDC (2431926,2431927) or as a part of ESI†.

The crystal structure of $Fe_{32+\delta}Ge_{35-x}P_x$ was used as a starting model for the $Fe_{32+\delta}Ge_{35-x}Si_x$ structure refinement. The P atoms which partially substitute Ge at the Ge1 site, hence the *x* in the formula, were replaced by Si atoms, as it was expected for the Si atoms to occupy the same position as P atoms due to their similar size. The crystal structure was then refined using the Jana2006 program.[25] The refinement of the first crystal from the $Fe_{32}Ge_{33}Si_2$ mixture converged to $x = 2.06(2)$ and $\delta = 0.598(6)$, the latter being the occupancy of the Fe5 site. This crystal will be hereafter referred to as $Fe_{32.6}Ge_{33}Si_2$. The second crystal from the $Fe_6Ge_4AlSi_2$ mixture was refined to a $Fe_{32.82(2)}Ge_{29.69(6)}Si_{5.31(6)}$ composition and will be referred to as $Fe_{32.8}Ge_{30}Si_5$. Given the low accuracy of the EDX analysis in our case, the larger crystals from the latter sample will be also referred to as the $Fe_{32.8}Ge_{30}Si_5$ crystals.

The refinement of the occupancies for other and Fe and Ge positions showed full occupation within the systematic error, except for Ge5, which occupancy is exactly ½, due to the symmetry of the structure (see section Crystal structure of $Fe_{32+\delta}Ge_{35-x}Si_x$ below). While the $Fe_{32+\delta}Ge_{35-x}P_x$ single crystal data show the presence of an additional Ge5' site (0.5, 0, 0) at 100 K,[20] this position cannot be resolved against the electronic density from the Ge5 atoms in $Fe_{32+\delta}Ge_{35-x}Si_x$, similarly to that in $Fe_{32+\delta}Ge_{33}As_2$.[19,20] Electronic density maps obtained by the maximum entropy method using the Dysnomia program[26] did not show electronic density maximum between two possible positions of the Ge5 atoms (Fig. 1).

Table 1 Summary of the results of the X-ray diffraction experiments for the $Fe_{32+\delta}Ge_{35-x}Si_x$ single crystals.

refined composition	$Fe_{32.598(6)}Ge_{32.94(2)}Si_{2.06(2)}$	$Fe_{32.82(2)}Ge_{29.69(6)}Si_{5.31(6)}$
EDX composition	$Fe_{32.54(12)}Ge_{32.83(14)}Si_{2.2(2)}$	$Fe_{32.65(14)}Ge_{29.13(7)}Si_{5.87(17)}$
molar weight	4269.4	4137.9
crystal system	hexagonal	
space group	*P6/mmm* (191)	
a, Å	11.8953(13)	11.8274(18)
c, Å	7.5446(8)	7.5597(11)
V, Å^3	924.52(17)	915.8(2)
Z	1	
ρ_{calc}, g/cm^3	7.6683	7.5027
radiation/ wavelength	Mo Kα/ 0.71073 Å	Ag Kα/ 0.56083 Å
temperature, K	100	293
sample form	truncated prism, 0.123×0.065×0.049 mm^3	truncated prism, 0.27×0.18×0.11 mm^3
absorption correction	Psi-scan	Psi-scan
colour	Metallic black	
θ range, °	3.35-32.04	2.13-24.95
h, k, l ranges	$-17 \le h \le 17$, $-17 \le k \le 17$, $-11 \le l \le 11$	$0 \le h \le 17$, $-17 \le k \le 3$, $0 \le l \le 11$
R_{int}	0.058	0.048
No. of parameters	49	49
No. of reflections	23449	2480
GoF	1.40	1.08
$\Delta\rho_{max}/\Delta\rho_{min}$, e/Å^3	1.98/−1.94	3.54/−2.62
$R_1[F^2 > 3\sigma(F^2)]$/ wR_2, %	1.65/1.99	2.81/4.19

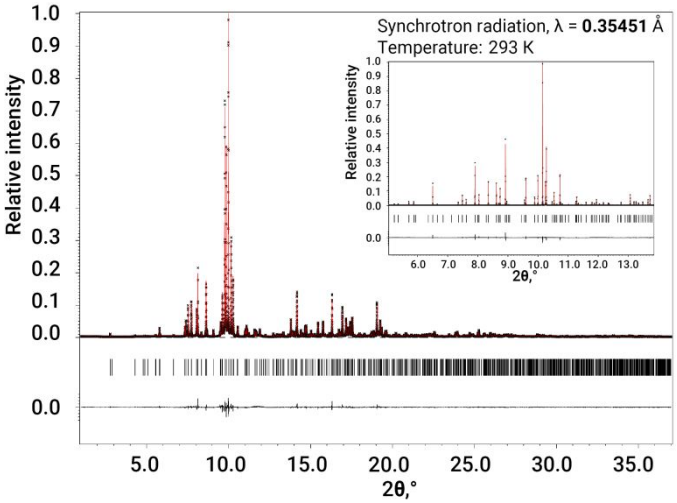

Fig. 2 High-resolution X-ray diffraction pattern of the $Fe_{32.7}Ge_{31}Si_4$ powder at room temperature. A closeup of the region between 5 and 13 degrees is shown in the inset. The experimental diffraction pattern is shown as black dots, the red line represents the calculated pattern. Peak positions are given by the black ticks. The difference plot is shown by the black curve at the bottom.

Selected powder samples ($Fe_{32.7}Ge_{31}Si_4$, $Fe_{32.7}Ge_{30}Si_5$, and $Fe_{32.7}Ge_{29}Si_6$) were studied by synchrotron high resolution powder diffraction (HRPD) at the ID 22 beamline of European Synchrotron Radiation Facility (ESRF) at room temperature. The diffracted rays were collected by nine Si [111] analyser crystals and an EIGER detector (EIGER2 X CdTe 2M-W).[28] Measurements were conducted on the sample enclosed in a glass capillary (0.4 mm diameter). The crystal structure was refined using the Rietveld method implemented in Jana2000 program.[29] The results of the powder refinement agreed well with the single crystal data. The experimental diffraction pattern for the $Fe_{32.7}Ge_{31}Si_4$ sample is given in Fig. 2. Details of the synchrotron HRPD experiments are summarized in Table S1 in ESI†. Atomic parameters for the $Fe_{32.7}Ge_{31}Si_4$ sample are given in Table S2 in ESI†. The crystallographic information files for the powder samples are available from CCDC (2431928–2431930) or as a part of ESI†.

Magnetic and heat capacity measurements

Magnetization of the $Fe_{32.7}Ge_{31}Si_4$ powder sample was measured with the VSM setup of the Physical Property Measurement System (PPMS, Quantum Design) in external

magnetic fields between 0.1 and 5 T in a temperature range 10−380 K. Heat capacity measurements were performed on the same $Fe_{32.7}Ge_{31}Si_4$ powder sample with the same PPMS device using HC option in a relaxation-type calorimeter in a temperature range of 2−170 K. Magnetization measurements of the $Fe_{32.8}Ge_{30}Si_5$ single crystal were performed using a squid magnetometer (MPMS 3, Quantum Design) in external magnetic fields up to 5 T in a temperature range of 2−300 K, while the measurements of the larger $Fe_{32.8}Ge_{30}Si_5$ twinned crystal was performed using the same squid magnetometer in magnetic fields up to 5 T in a temperature range of 250−380 K.

Results and discussion

Synthesis, crystal growth and homogeneity range of $Fe_{32+\delta}Ge_{35-x}Si_x$

While both $Fe_{32+\delta}Ge_{33}As_2$ and $Fe_{32+\delta}Ge_{35-x}P_x$ could be obtained by a straightforward two-step synthesis from the elements,[19,20] this technique had found to be unsuitable for $Fe_{32+\delta}Ge_{35-x}Si_x$, as it yielded unreacted Si and binary iron germanides. Solid state reaction between the elements at 650-800°C resulted in the formation of cubic $FeGe_{1-x}Si_x$ solid solution, $FeGe_2$, and only a small amount of the target phase. Thus, a different technique was developed for the synthesis of $Fe_{32+\delta}Ge_{35-x}Si_x$. The compound was successfully obtained by a solid-state reaction at 800°C of Fe_5Si_3, FeGe, and $FeGe_2$, which sidestepped the formation of the inert $FeGe_{1-x}Si_x$ cubic phase during the synthesis.

Likely due to a slight excess of iron in the Fe_5Si_3 sample, the obtained $Fe_{32+\delta}Ge_{35-x}Si_x$ powder samples contain slightly higher amount of iron than expected, which is indicated by the structural analysis (Tables S1 and S2 in ESI†) and the presence of η-$Fe_{7-\delta}Ge_4$ in the samples with a lower Si load (Fig. S1 in ESI†) or $FeGe_{1-x}Si_x$ in the samples with a higher Si load.

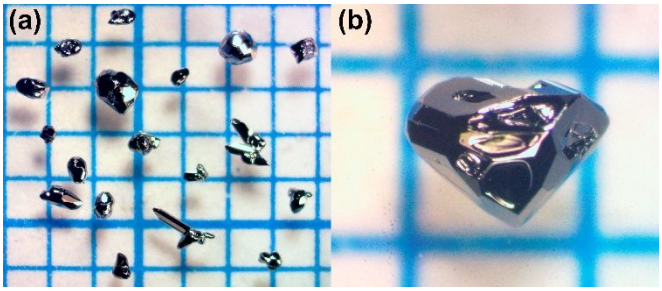

Fig. 3 Crystals of $Fe_{32+\delta}Ge_{35-x}Si_x$ grown from the $Fe_6Ge_4AlSi_2$ mixture using iodine as the transport agent: several clumps and twinned needles (a), closeup of a heart-shaped twinned crystal (b).

The single crystal growth, while is fairly simple to implement, also have its peculiarities. The single crystals of $Fe_{32+\delta}Ge_{35-x}Si_x$ can be grown using chemical vapor transport reactions both from the $Fe_{32+\delta}Ge_{35-x}Si_x$ powder as well as the elements using iodine as a transport agent. The black hexagonal needles or clumps of twinned needles with glossy surface are formed during the annealing. Unexpectedly, the use of a temperature gradient at low temperatures seem to hinder the formation of the target phase, as only small crystals could be obtained even after a month of annealing. As a by-product of the synthesis, the crystals of the ferromagnetic η-$Fe_{7-\delta}Ge_4$ were formed, which are similar in appearance to the crystals of $Fe_{32+\delta}Ge_{35-x}Si_x$.

Well defined crystals of $Fe_{32+\delta}Ge_{35-x}Si_x$ can be obtained using non-stoichiometric mixtures of the elements with an excess of Si at elevated temperatures above 700°C. Larger crystals (Fig. 3), however, were grown by adding Al into the initial mixture to reduce silicon from the tube walls, as it is highly active and facilitates the formation of $Fe_{32+\delta}Ge_{35-x}Si_x$ crystals. Using these techniques, the Ge and $FeGe_{1-x}Si_x$ crystals are formed as a by-product. The Ge crystals can be easily sorted out due to their distinct appearance with a rhombic dodecahedron shape and a grey matte surface. Although, the $FeGe_{1-x}Si_x$ crystals are quite similar to $Fe_{32+\delta}Ge_{35-x}Si_x$ in appearance, the former can be also somewhat consistently separated from those of the target phase by large and well-defined trigonal edges of the $FeGe_{1-x}Si_x$ crystals.

The compound demonstrates a significant homogeneity range

Table 2 Atomic parameters for the $Fe_{32.6}Ge_{33}Si_2$ single crystal at T = 100 K and the $Fe_{32.8}Ge_{30}Si_5$ single crystal at T = 293 K.

			$Fe_{32.6}Ge_{33}Si_2$ single crystal at T = 100 K				$Fe_{32.8}Ge_{30}Si_5$ single crystal at T = 293 K			
Atom	Wyck.	y	x	z	U_{eq}, Å^2	Occ.	x	z	U_{eq}, Å^2	Occ.
Fe1	6*m*	2*x*	0.21109(3)	1/2	0.0020(2)	1	0.20989(7)	1/2	0.0044(4)	1
Fe2	2*c*	2/3	1/3	0	0.0059(3)	1	1/3	0	0.0075(6)	1
Fe3	12*n*	0	0.38552(4)	0.28057(7)	0.00389(16)	1	0.38308(10)	0.28077(16)	0.0073(3)	1
Fe4	12*o*	2*x*	0.12337(2)	0.23590(6)	0.00216(16)	1	0.12273(5)	0.24057(15)	0.0055(3)	1
Fe5	1*b*	0	0	1/2	0.0051(8)	0.598(6)	0	1/2	0.0104(14)	0.83(2)
Ge0	2*e*	0	0	0.16405(12)	0.0033(2)	1	0	0.1624(3)	0.0069(4)	1
Ge1	6*k*	0	0.22798(6)	1/2	0.0018(2)	0.656(4)	0.2270(2)	1/2	0.0049(8)	0.115(10)
Si1	6*k*	0	0.22798(6)	1/2	0.0018(2)	0.344(4)	0.2270(2)	1/2	0.0049(8)	0.885(10)
Ge2	6*m*	1−*x*	0.43107(3)	1/2	0.00310(16)	1	0.43145(6)	1/2	0.0072(3)	1
Ge3	12*o*	2*x*	0.244422(19)	0.19671(5)	0.00895(13)	1	0.24432(4)	0.19710(11)	0.0120(3)	1
Ge4	6*j*	0	0.27393(5)	0	0.00294(16)	1	0.27023(10)	0	0.0073(3)	1
Ge5	6*l*	1−*x*	0.47425(7)	0	0.0154(4)	0.5	0.47702(16)	0	0.5	0.5

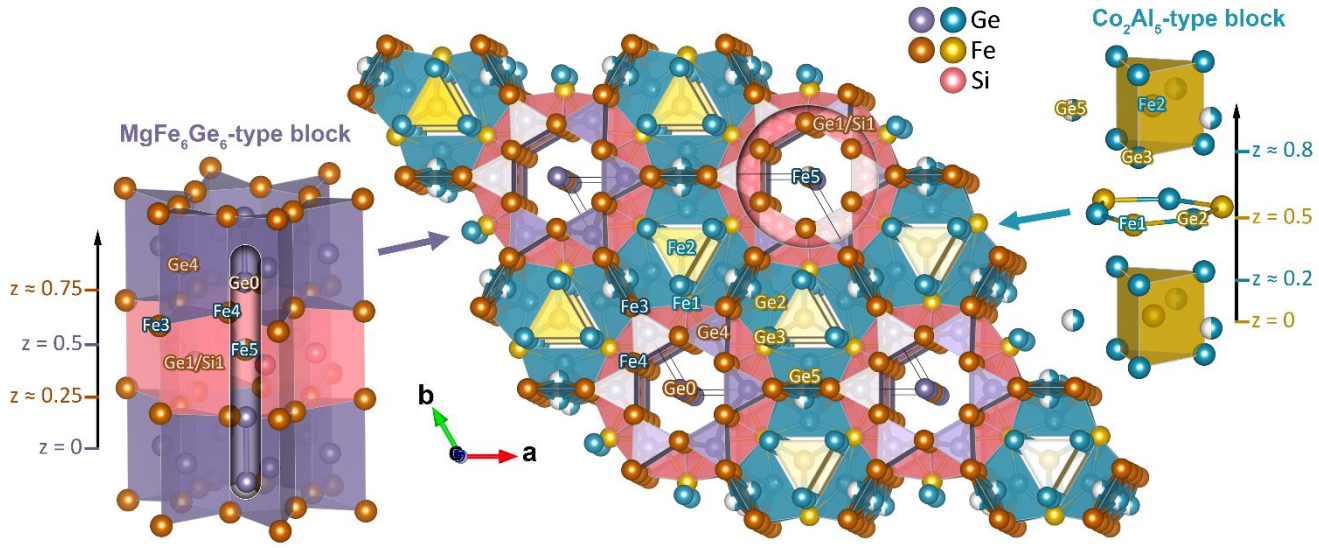

Fig. 4 Polyhedral view of the crystal structure of $Fe_{32+\delta}Ge_{35-x}Si_x$ (middle) along with its basic structure blocks: $MgFe_6Ge_6$-type column (left) and Co_2Al_5-type column (right).

due to variations in both the Fe content (δ) and the level of Ge to Si substitution (*x*). At 800°C, *x* could vary in the range of 2-5.5, while δ was found in the range of 0.8-1 at this temperature. Due to slow reaction rate, the homogeneity range at lower temperature might be difficult to establish. However, the composition of the single crystal $Fe_{32.6}Ge_{33}Si_2$ obtained at 650°C indicates that the Fe content might be shifted to lower values at lower temperatures.

Crystal structure of $Fe_{32+\delta}Ge_{35-x}Si_x$

$Fe_{32+\delta}Ge_{35-x}Si_x$ crystallizes in the hexagonal crystal system in the *P6/mmm* space group (*a* = 11.87351(4), *b* = 7.58509(3) for δ = 0.8 and *x* = 5). Our structural analysis shows that $Fe_{32+\delta}Ge_{35-x}Si_x$ is isomorphous to $Fe_{32+\delta}Ge_{33}As_2$ and $Fe_{32+\delta}Ge_{35-x}P_x$ previously characterized by our group.[19-21] Since their structures were discussed extensively in the previous papers,[19,20] we will limit the description of the $Fe_{32+\delta}Ge_{35-x}Si_x$ crystal structure to its most important features.

$Fe_{32+\delta}Ge_{35-x}Si_x$ features a complex two-dimensional intergrowth[30] of $MgFe_6Ge_6$[22] (also known as $HfFe_6Ge_6$)[31] and Co_2Al_5[23] structure types, which are represented by infinite columns forming a mosaic in the *ab* plane (Fig. 4). The compound has 5 Fe sites, 5 Ge sites, and one mixed Ge/Si site. The Fe3, Fe4, Fe5, Ge0, Ge1, and Ge4 sites belong to the $MgFe_6Ge_6$-type block, while the Fe1, Fe2, Ge2, Ge3, and Ge5 sites belong to the Co_2Al_5-type block (Table 2). Si atoms partially substitute Ge at the Ge1 site inside the $MgFe_6Ge_6$-type block.

The $MgFe_6Ge_6$-type block (Fig. 4) consists of vertical stacks of trigonal prisms $GeFe_6$ surrounding hexagonal channels, inside of which the Ge_2 dumbbells are alternating with Fe atoms or Fe vacancies in the partially occupied Fe5 site. The occupancy of the latter corresponds to δ in the formula and can vary in the range of 0.6-1. The Co_2Al_5-type block (Fig. 4) is comprised of $FeGe_6$ isolated trigonal prisms, Fe1-Ge2 6-membered rings placed between them, and Ge5 atoms adjacent to the former. The latter site, Ge5, is particularly interesting, as it is located at the intersection of two Co_2Al_5-type blocks leading to its halved occupancy. The Ge5 atoms can be on the either side of the mirror plane, but not on both, since the latter would create improbably short Ge-Ge distances *ca.* 1 Å.

The inclusion of the Co_2Al_5-type columns breaks the kagome nets of Fe atoms inherited from $MgFe_6Ge_6$ into hexagrams (Fig. 5a) that form trigonal lattice and are connected by quite long Fe3-Fe3 bonds (2.7-2.8 Å) creating a (3.9^2;3.6.3.9) tiling (Fig. 5b) at *z* ≈ 0.25 and 0.75. As a result of the size mismatch between two blocks, the hexagrams are also not planar and have a bowl-like shape. Despite the fragmentation of the kagome lattice, the geometry of the resulting Fe net still preserves magnetic frustration.

While fragmenting the parent kagome lattice at *z* ≈ 0.25 and 0.75, the inclusion of the Co_2Al_5-type block creates another frustrated Fe nets at *z* = 0 and *z* = 0.5. At *z* = 0.5, Fe1 and Fe5 atoms separated by 4.3-4.4 Å form (3^6;3^2.4.3.4) nets (Fig. 5c). At *z* = 0, one can also discern honeycomb or (6^3) nets of the Fe2 atoms separated by a distance of 6.8-6.9 Å depending on the composition (Fig. 5d). While inside the nets, Fe1, Fe2, and Fe5 atoms are spread quite far apart, these atoms are close to the Fe3 and Fe4 atoms from the neighbouring layers. In particular, Fe1 atoms are separated by only 2.65 Å from the Fe4 atoms.

If one considers an array of such close Fe-Fe contacts, it reveals a quite different picture of the Fe network. The Fe1, Fe3 and Fe4 atoms form doughnut-shaped cages, which are loosely connected into layers by Fe3-Fe3 bonds (Fig. 6). The Fe5 atoms located inside the cages (Fig. 6c) are separated from the nearest Fe atoms (Fe4) by large distances of 3.1-3.2 Å depending on the composition. The Fe2 atoms are practically isolated from the rest of the Fe network with the closest Fe2-Fe distance being the Fe2-Fe4 separation of 4.3 Å.

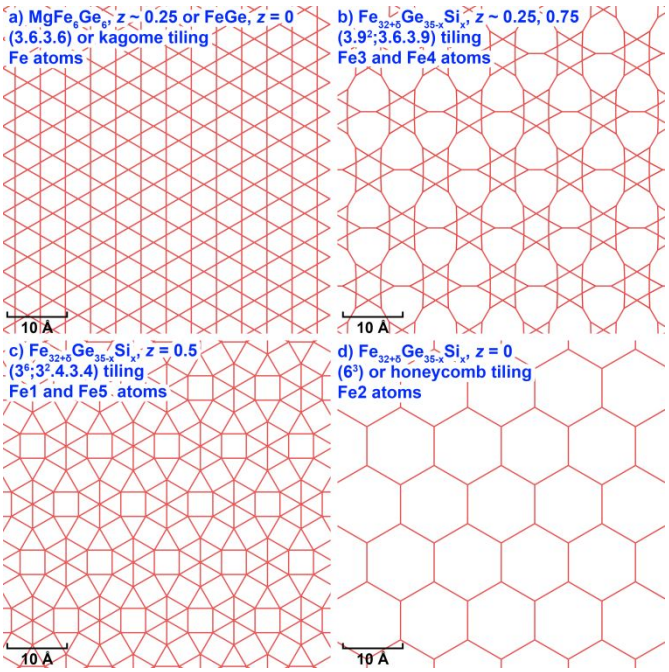

Fig. 5 Fe nets in the crystal structure of $MgFe_6Ge_6$ (a) and $Fe_{32+\delta}Ge_{35-x}Si_x$ (c-d).

Despite the presence of Si atoms and noticeable distortion, the Fe-Ge and Fe-Fe contacts within the $MgFe_6Ge_6$-type block and on its boundary (Table S1 and Fig. S2 in ESI†) mostly remain on the upper end of a typical range of interatomic distances in these pairs (2.5–2.7 Å).[32–38] The Fe-Si distances and the atomic environment of the Si1 atoms are also quite typical, being 2.4-2.7 Å.[39-43] A slightly distorted version of the Si1 polyhedron can be found in Fe_5Si_3 (Fig. 7).[40] As the Si content increases, the Ge1/Si1 polyhedron expectedly contracts (Fig. S2 in ESI†).

The Co_2Al_5-type block, on the other hand, mostly retains its geometry from the structure prototype including very short bonds between *d*- and *p*-element atoms. The Fe2-Ge3 distances are 2.36 Å, while the Fe1-Ge2 distance is only 2.31 Å. Such short Fe-Ge distances are very rare and were observed only in a handful of compounds besides the other two family members:[19–21] Fe_2Ge_3,[32] $LaFeGe_3$,[44] and $CeFeGe_3$.[45]

Although $Fe_{32+\delta}Ge_{35-x}Si_x$ is isomorphous to $Fe_{32+\delta}Ge_{33}As_2$ and $Fe_{32+\delta}Ge_{35-x}P_x$, there are notable differences in the crystal structures of compounds. The Si atoms in $Fe_{32+\delta}Ge_{35-x}Si_x$ occupy the same Ge1 site as P atoms in $Fe_{32+\delta}Ge_{35-x}P_x$, whereas in $Fe_{32+\delta}Ge_{33}As_2$, As atoms replace Ge atoms at the Ge0 site forming As_2 dumbbells (Fig. 8).[19-21] Such a strong preference for a specific position comes from the difference in electronic configurations of As, P, and Si and the crucial roles that these atoms play in the stabilisation of the compounds, as will be shown below.

Based on the crystal structure analysis of $Fe_{32+\delta}Ge_{33}As_2$ and $Fe_{32+\delta}Ge_{35-x}P_x$, we have shown that the substitution of Ge by both P and As, despite their different positions in the structure, relieves the stress at the Fe1-Ge1 boundary between the $MgFe_6Ge_6$-type and Co_2Al_5-type blocks.[19,20] The As substitution achieves that by removing most of Fe atoms from the Fe5 site, due to the greater number of valence electrons of As atoms in

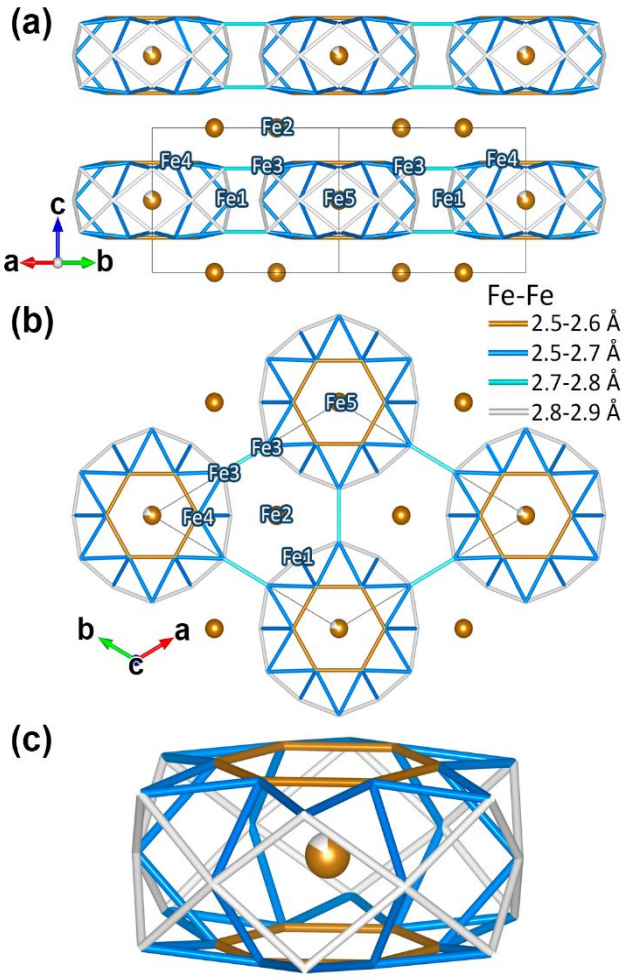

Fig. 6 Network of close Fe-Fe contacts in the crystal structure of $Fe_{32+\delta}Ge_{35-x}Si_x$: [1 −1 0] projection (a), *ab*-projection (b), and the single cage of Fe atoms (Fe1, Fe3, Fe4), inside of which partially occupied Fe5 site is located (c). The Fe-Fe distances correspond to those in the $Fe_{32.8}Ge_{30}Si_5$ single crystal at 293 K.

comparison with that of Ge atoms. This allows Ge1 atoms to shift further inside the $MgFe_6Ge_6$-type block. The P atoms resolve the stress in a more direct way – by simply substituting the Ge atoms at the Ge1 site, which reduces the effective size of the atom in this position. Given that the Si atoms are also found in the same position as the P atoms, we assume that a similar mechanism should be in play for Si atoms.

The comparison of the interatomic distances in $Fe_{32.1}Ge_{33}As_2$, $Fe_{32.6}Ge_{33}P_2$, and $Fe_{32.6}Ge_{33}Si_2$ (Table S1 and Fig. S3 in ESI†) shows that $Fe_{32+\delta}Ge_{35-x}Si_x$ finds itself somewhere midway between $Fe_{32+\delta}Ge_{33}As_2$ and $Fe_{32+\delta}Ge_{35-x}P_x$ for $x = 2$. In particular, since Si is in between Ge and P in terms of its atomic size,[46] Ge1-Fe distances decrease upon Si doping but not as much as in the case of P (Fig. S3 in ESI†),[20] except for the Ge1–Fe5 distance, which is surprisingly shorter in $Fe_{32+\delta}Ge_{35-x}Si_x$ than in $Fe_{32+\delta}Ge_{35-x}P_x$ and even in $Fe_{32+\delta}Ge_{33}As_2$, despite a much lower Fe5 occupancy in the former. The difference in interatomic distances also translates to the difference in the unit cell volume, the latter decreasing along the $Fe_{32.1}Ge_{33}As_2$–$Fe_{32.6}Ge_{33}Si_2$–$Fe_{32.6}Ge_{33}P_2$ sequence.

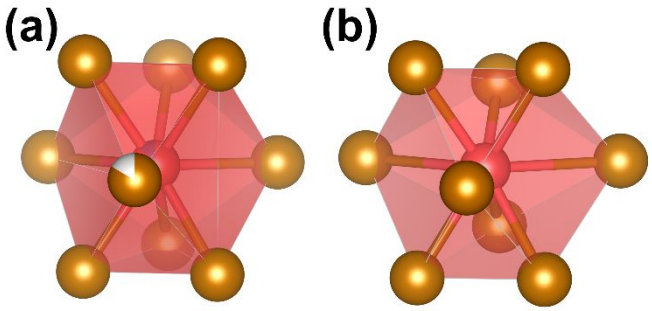

Fig. 7 The Ge1/Si1 polyhedron in the crystal structure of $Fe_{32+\delta}Ge_{35-x}Si_x$ (a) and the Si polyhedron in Fe_5Si_3 (b).[40]

The shorter Ge1–Fe5 distance in the case of $Fe_{32+\delta}Ge_{35-x}Si_x$, means that the Ge1/Si1 atoms are shifted towards the centre of the $MgFe_6Ge_6$-type block and are also closer to each other, since the Ge1–Fe5 and Ge1–Ge1 distances are identical, due to the hexagonal symmetry of the structure. The shift of Si atoms towards the centre of the $MgFe_6Ge_6$-type block also results in a noticeable decrease in the *a* parameter comparable to that of $Fe_{32+\delta}Ge_{35-x}P_x$ and an increase of the *c* parameter even in comparison with $Fe_{32+\delta}Ge_{33}As_2$ (Fig. S3 in ESI†).

An increase in the Si content expectedly leads to a decrease of the Ge1–Fe distances, including the Ge1–Fe5 distance (Table S1 and Fig. S2 in ESI†), which results in the further shift of the Ge1/Si1 atoms towards the centre of the $MgFe_6Ge_6$-type block, despite the greater occupancy of the Fe5 site. Because of that, the increase in the Si concentration leads to the further decrease of the *a* parameter (Fig. S2 in ESI†). Interestingly, the *c* parameter also decreases upon further Si doping due to an almost isotropic decrease of the Ge1–Fe distances (Fig. S2 in ESI†), which contracts the Ge1/Si1 polyhedron in the *c* direction as well.

It is interesting to note that the P doping results in the Ge1 atoms moving in the opposite direction – towards the edge of the $MgFe_6Ge_6$-type block.[20,47] While the decrease in interatomic distances is expected for the Si atoms, given the smaller atomic size of Si compared with Ge, the increase in the Ge1–Fe5 and Ge1–Ge1 distances upon P doping goes against this reasoning. The different effect of Si and P on the Ge1–Fe5 and Ge1–Ge1 distances might stem from their different valencies. We have previously shown in the case of the related Fe_6Ge_5 and α-Fe_6Ga_5 phases[37,48] that the increase in the number of valence electrons for *p*-element E leads to stronger Fe-E interactions making E-E interactions to be less bonding in nature, which draws *p*-element atoms away from each other.

The shift of the Ge1/Si1 atoms towards the centre of the $MgFe_6Ge_6$-type block provides an additional space for the Ge2–Fe1 rings. Thus, in addition to the reduction of the Ge1/Si1–Fe1 distances, the Si substitution provides another important structural change beneficial to the stabilisation of the intergrowth structure. Fig. 9 shows how both effects work in tandem providing necessary space for the Ge2-Fe1 rings. Since the Ge1/Si1–Fe1 distance is larger than the Ge1/P1–Fe1 distance (Table S1 in ESI†), the shift of the Ge1/Si1 atoms towards the centre of the column might be essential to stabilise the structure of $Fe_{32+\delta}Ge_{35-x}Si_x$ at lower levels of the Si-doping.

The differences in electronic configurations of As, P, and Si give rise to another important structural distinction between the phases. The occupancy of the Fe5 site (δ) in $Fe_{32+\delta}Ge_{33}As_2$ did not exceed 0.14,[19,21] due to the formation of the neighbouring As_2 dumbbells. $Fe_{32+\delta}Ge_{35-x}P_x$ features Ge_2 dumbbells in place of the As_2 ones (Fig. 8), which allows for a much higher occupancy of the Fe5 site. Structural investigations of $Fe_{32+\delta}Ge_{35-x}P_x$ shows the occupancy of Fe5 to be in the range of 0.5-0.6[20,21,47] and virtually independent of the Ge/P ratio at the neighbouring Ge1/P1 site. While $Fe_{32+\delta}Ge_{35-x}Si_x$ also features only Ge_2 dumbbells, the Si doping in $Fe_{32+\delta}Ge_{35-x}Si_x$ allows for an even higher occupancy of the Fe5 site (δ = 0.6–1), which tends to increase with the increasing Si content in the phase and can even reach unity at higher Si concentrations (Tables S2 and S3 in ESI†).

The exact reason for such a different effect of P and Si doping on the Fe5 occupancy is hard to pinpoint. Two factors can be at play here. Due to one additional electron on the P atoms, the presence of Fe5 atoms could destabilise the bonding of the P1 atoms with its neighbours. However, previous ^{31}P NMR studies of the $Fe_{32+\delta}Ge_{35-x}P_x$ local structure have shown that the distribution of Fe atoms and Fe vacancies at the Fe5 site is practically independent of the P/Ge distribution at the neighbouring Ge1 site.[20] The second possible reason is the heavy compression of the unit cell in the *c* direction[20,47] along the (-Fe5-Ge0-Ge0-) chain, which does not occur in $Fe_{32+\delta}Ge_{35-x}Si_x$ (Fig. S2 and S3 in ESI†), due to the shift of the Si

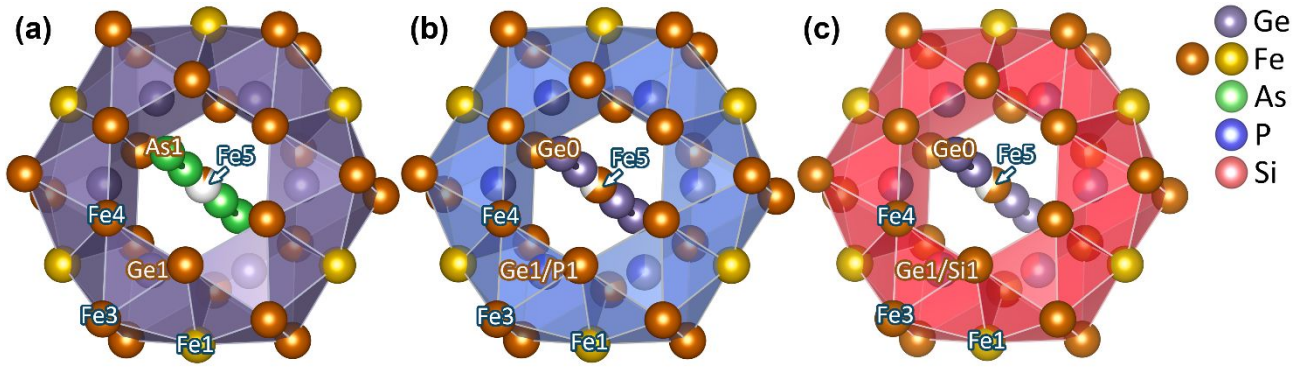

Fig. 8 Comparison of the central fragments of the $MgFe_6Ge_6$-type block in the crystal structures of $Fe_{32.1}Ge_{33}As_2$[19] (a), $Fe_{32.6}Ge_{33}P_2$[20] (b), and $Fe_{32.6}Ge_{33}Si_2$ (c), showing the positions of As, P, and Si in their respective phases.

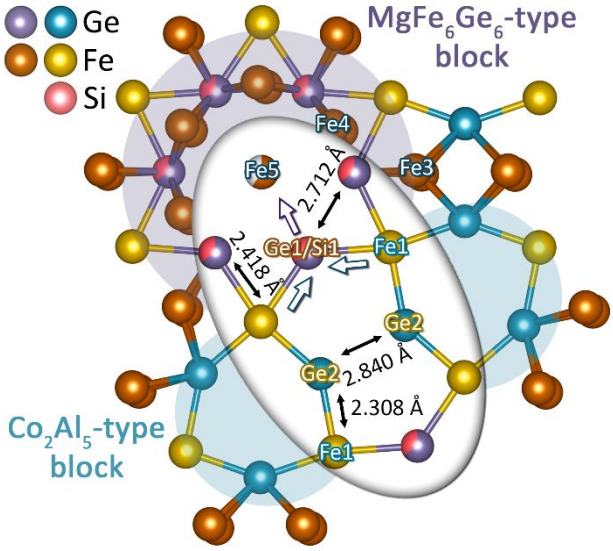

Fig. 9 A closeup of the boundary between $MgFe_6Ge_6$-type and Co_2Al_5-type blocks in the crystal structure of $Fe_{32.6}Ge_{33}Si_2$ at 100 K. The standard errors are not displayed and are within 0.001 Å. The arrows represent the shifts of the Fe and Ge atoms with respect to their positions in $Fe_{32.1}Ge_{33}As_2$ at the same temperature.[19]

atoms towards the centre of the $MgFe_6Ge_6$-type block.

The combination of the larger size of the Si atoms compared to that of the P atoms and the shift of the Si atoms towards the centre of the column results in another interesting structural difference between $Fe_{32+\delta}Ge_{35-x}Si_x$ and $Fe_{32+\delta}Ge_{35-x}P_x$. One of the distinctive features of $Fe_{32+\delta}Ge_{35-x}P_x$ is the formation of an additional partially occupied Ge5' site (0.5, 0, 0) in between two possible positions of the Ge5 atom at low temperatures.[20] This occurs due to a large separation between Ge4 and Ge5 atoms, as the Ge4 atoms are forced to move towards the centre of the $MgFe_6Ge_6$-type block, due to the shift of the neighbouring Fe4 atoms along the *c* axis towards the Ge1/P1 atoms.[20]

Using the same experimental setup and the $Fe_{32+\delta}Ge_{35-x}Si_x$ single crystal with the same level of Ge substitution (x = 2) does not reveal the presence of an additional Ge5' site. In the case of $Fe_{32+\delta}Ge_{35-x}Si_x$, the Fe4 atoms and consequently the Ge4 atoms are closer to their positions in $Fe_{32+\delta}Ge_{33}As_2$, ensuring smaller Ge4-Ge5 separation and preventing the segregation of Ge atoms into the Ge5' site (Fig. 10).

Magnetic properties of $Fe_{32+\delta}Ge_{35-x}Si_x$

Magnetic measurements of the $Fe_{32.8}Ge_{30}Si_5$ single crystal revealed a complicated magnetic behaviour. Temperature and field dependence of magnetization is presented in Fig. 11. Above 225 K, the compound displays Curie-Weiss behaviour with an effective magnetic moment near 3 μ_B/Fe and a large negative Weiss temperature below −500 K (Fig. S4 and S5 in ESI†). The latter clearly indicates significant antiferromagnetic interactions. The single crystal does not show a pronounced magnetic anisotropy in this region since the magnetisation is very similar between different orientations of the crystal (Fig. S6 in ESI†).

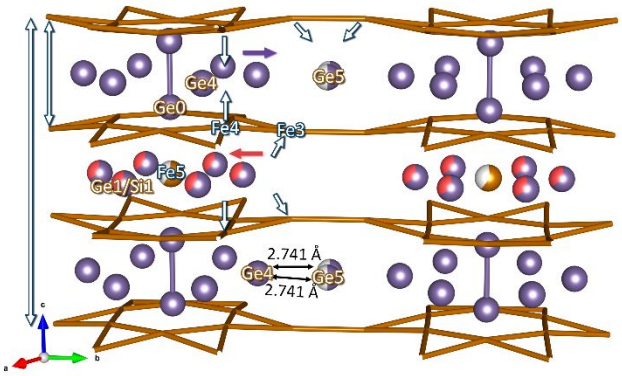

Fig. 10 Two neighbouring columns of the $MgFe_6Ge_6$ structure type in the crystal structure of $Fe_{32.6}Ge_{33}Si_2$ at 100 K. The standard errors are not shown and are within 0.001 Å. The arrows represent the shifts of the Fe and Ge atoms with respect to their positions in the structure of $Fe_{32.6}Ge_{33}P_2$ at the same temperature.[20] The white arrows represent the shifts of the Fe atoms, while the coloured ones show the shifts of the *p*-element atoms.

Upon further cooling, the susceptibility reaches its maximum around 180 K and gradually decreases afterwards (Fig. 11a). Below 180 K, we observe a different behaviour for different orientations of the magnetic field. When the magnetic field is parallel to the *c* axis, the magnetic susceptibility $\chi_{||}(T)$ gradually declines as the temperature decreases until a sharp drop at 70-80 K depending on the field strength. Below the $\chi_{||}(T)$ drop, the susceptibility continues its slow decrease. While the increase in $\mu_0 H$ from 0.1 to 1 T leads to decreasing the temperature of the $\chi_{||}$ drop only slightly, the increase of $\mu_0 H$ from 1 to 5 T moves it further down by 10 K (Fig. 11b). Aside from the change in the temperature of the $\chi_{||}$ drop, the magnetic field has no further effect on the $\chi_{||}(T)$ curves.

The opposite seems to be true if the magnetic field is applied in the direction perpendicular to the *c* axis, or parallel to the *ab* plane. While also declining, the *ab* susceptibility or $\chi_{⎚}$ depends heavily on the magnetic field between 80 and 150 K and steadily increases with the increasing field. Below 80 K, $\chi_{⎚}$ rapidly increases in 0.1 and 1 T fields upon cooling and converges to the 5 T curve, which experience only a small kink in this region. At low temperatures, one can also observe a slight reduction of $\chi_{⎚}$ upon cooling below 10 K in 0.1 T field, which is suppressed by the application of stronger magnetic fields. Peculiarly, no anomalies are present in this low temperature region for $\chi_{||}$. The difference in the magnetic behaviour below 80 K between two orientations of the crystal is also clearly seen in the field dependence of the low temperature magnetisation $M(H)$ (Fig. 11d), especially in contrast to the $M(H)$ curves at 100 K and 300 K, which appear much closer together for these orientations (Fig. S6 in ESI†).

The described above behaviour appears to be a well-defined case of an antiferromagnet, which experiences partial or complete reorientation of magnetic moments induced both by application of magnetic field and change in temperature. While each $\chi(T)$ curve on its own cannot be used to estimate the Neel temperature, since the $\chi(T)$ maximum around 180 K is quite broad, the divergence of the $\chi_{⎚}(T)$ curves for different fields near 150 K indicates the latter as the transition temperature.

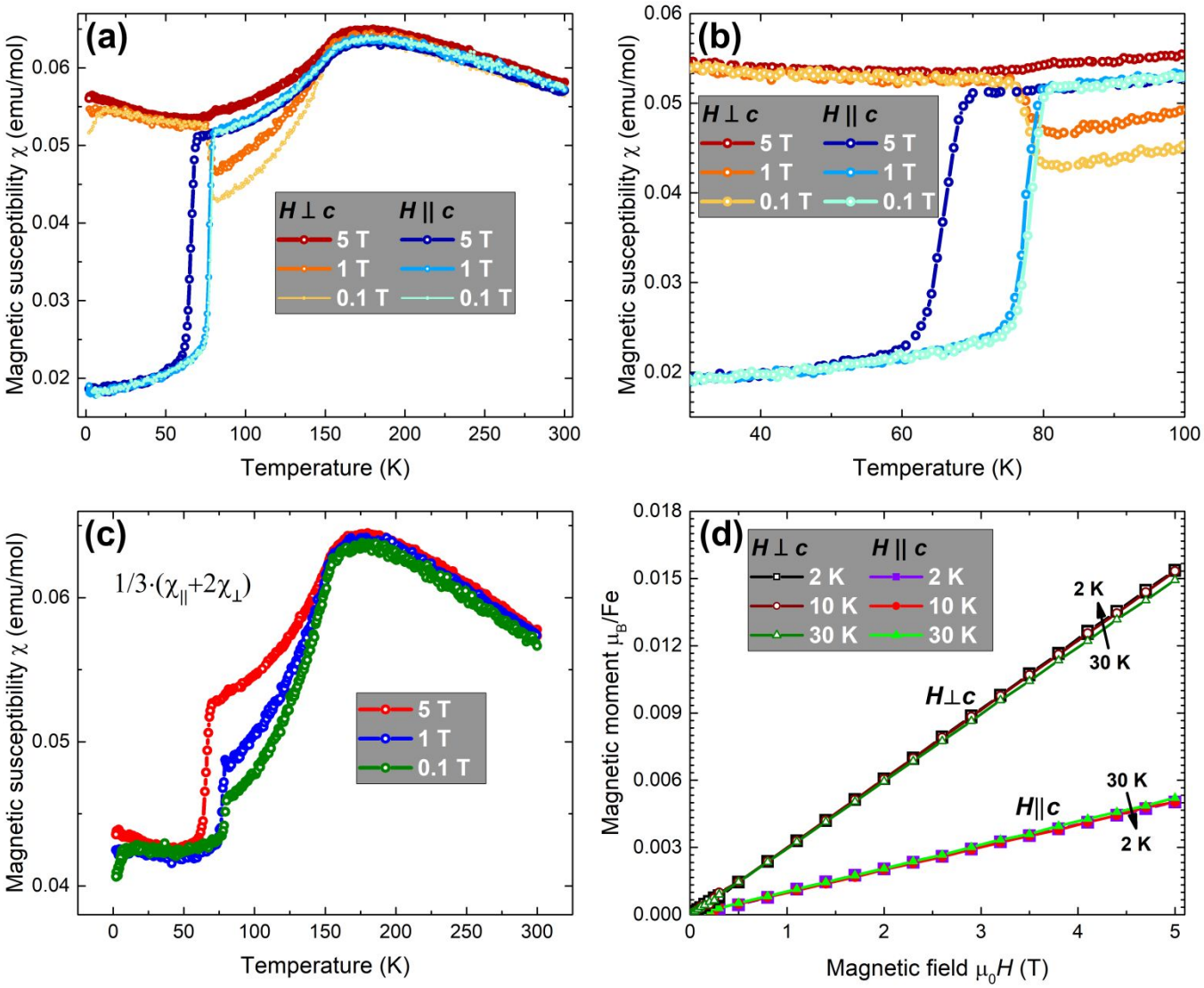

Fig. 11 Magnetic behaviour of the $Fe_{32.8}Ge_{30}Si_5$ single crystal: magnetic susceptibility in various magnetic fields of $\mu_0 H$ = 0.1–5 T applied along the *c* axis or perpendicular to it (a), closeup of a region between 30 and 100 K (b), the averaged susceptibility simulating a powder magnetic response (c), field dependence of low temperature magnetization (d).

The divergence of the $\chi_{⎚}(T)$ curves occurs due to a gradual reorientation of the antiferromagnetically coupled moments from the *ab* plane towards the *c* axis, as the magnetic field increases. As the spins rotate towards the *c* axis, they become less strongly coupled in the *ab* plane resulting in the $\chi_{⎚}$ increase.[49] Below 80 K in 0.1 and 1 T fields, the magnetic moments rapidly rotate from the *ab* plane towards the *c* axis upon cooling, which causes the sharp drop of $\chi_{||}$ and a similar upturn in $\chi_{⎚}$. If the strong magnetic field $\mu_0 H$ = 5 T is applied to the *ab* plane, the magnetic moments involved in the reorientation become fully locked along the *c* axis right from the onset of the antiferromagnetic ordering, hence we observe only small changes to $\chi_{⎚}$ near 80 K. The application of magnetic field to the *c* axis stabilises the in-plane configuration of the magnetic moments and pushes the temperature of spin reorientation T_{SR} to lower temperatures.

The decrease in $\chi_{⎚}$ at low temperatures does not appear to be caused by spin reorientation, as there is no opposite effect for $\chi_{||}$. The possible explanation is the antiferromagnetic ordering of the *ab*-component of Fe magnetic moments, which remain disordered at higher temperatures.

The drastic difference between the absolute values of Weiss and Neel temperatures ($|\theta w|/T_N > 3$) also indicates a significant degree of magnetic frustration, preventing long range magnetic ordering to form at higher temperatures. The magnetic frustration does not only diminish the Neel temperature, but it also causes a negative deviation from Curie-Weiss behaviour above T_N as spins become strongly coupled. Similar negative deviations from Curie-Weiss behaviour usually occur in magnetic systems with strong antiferromagnetic coupling in low-dimensional fragments.[50-52]

The common cause of the magnetic frustration is the presence of trigonal atomic fragments with dominating antiferromagnetic interactions between individual atoms. As it was shown in the crystal structure discussion above, the Fe sublattice in $Fe_{32+\delta}Ge_{35-x}Si_x$ is composed of a large number of geometrically frustrated trigonal fragments inherited from both parent structures and conserved due to hexagonal symmetry of

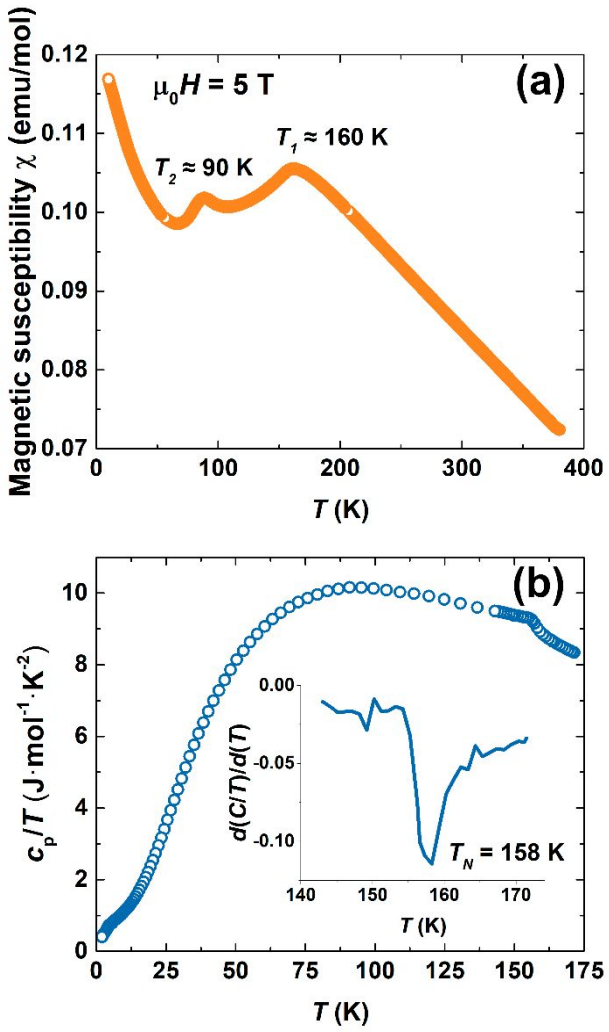

Fig. 12 Temperature dependence of the magnetic susceptibility of the $Fe_{32.7}Ge_{31}Si_4$ powder in an applied field of $\mu_0 H$ = 5 T (a) and the heat capacity divided by temperature of the same $Fe_{32.7}Ge_{31}Si_4$ powder in zero magnetic field (b). The inset (b) shows temperature derivative of the heat capacity divided by temperature.

the resulting structure. The Fe atoms are also connected through a large number of Ge atoms, which can serve as a medium for the antiferromagnetic superexchange interactions in iron germanides.[53]

High degree of the magnetic frustration also becomes apparent in comparison with the related iron germanides, in which the kagome nets of Fe atoms are conserved. The examples are $MgFe_6Ge_6$-type phases and the related ones, including hexagonal FeGe, which is the parent structure of $MgFe_6Ge_6$. The ordering temperatures for these compounds rarely fall below 400 K.[54-72] It is worth nothing that the competition of the magnetic interactions still manifests itself even in these cases. Deviation from the collinear ordering in the Fe sublattice is quite common in these compounds at low temperatures.[55,56,58,66-71] Some phases including $YbFe_6Ge_6$ and $FeGe_{1-x}Sb_x$ also exhibit complete spin reorientation.[57,58,71,72]

In addition to the study of the single crystal, we have performed similar magnetic measurements on the $Fe_{32.7}Ge_{31}Si_4$ powder sample, which showed that the main features of magnetic behaviour of the single crystal are reproduced in the polycrystalline powder. Magnetic susceptibility of the $Fe_{32.7}Ge_{31}Si_4$ powder sample shows a maximum at 160 K near T_N and a sharp drop at 90 K, near T_{SR} (Fig. 12a). Due to a minor ferromagnetic impurity of η-$Fe_{7-\delta}Ge_4$,[73] the antiferromagnetic behaviour of $Fe_{32+\delta}Ge_{35-x}Si_x$ becomes apparent only in strong fields (Fig. S7 in ESI†). There is also an upturn of the susceptibility at low temperatures, likely due to the same impurity or due to paramagnetic centres at the surface of the particles. Except for the latter, the $\chi(T)$ for the $Fe_{32.7}Ge_{31}Si_4$ powder matches the averaged single crystal susceptibility quite well (see Fig. 11c).

Heat capacity data of the same $Fe_{32+\delta}Ge_{35-x}Si_x$ powder sample in zero field shows a second order transition occurring at 158 K, while no anomaly near T_{SR} can be distinguished (Fig. 12b). Given the drastic changes to orientation of magnetic moments, a clear indication of the phase transition in the heat capacity data could be expected. It is worth noting, however, that no anomaly at its respective T_{SR} was observed in the heat capacity measurements of $Fe_{32+\delta}Ge_{33}As_2$.[19,21] No anomalies were observed also in the case of the related solid solution $FeGe_{1-x}Sb_x$, which also demonstrates spin reorientation below T_N.[71,72] The absence of the pronounced heat capacity anomaly could be due to several reasons. Spin reorientation could affect only a small portion of the Fe substructure, as it was the case for $Fe_{32+\delta}Ge_{33}As_2$ and $Fe_{32+\delta}Ge_{35-x}P_x$,[19,21] thus not producing a large specific heat effect. Spin reorientation may also occur gradually, in a way similar to that in $Fe_{32+\delta}Ge_{35-x}P_x$, resulting in a smooth and broad heat capacity peak indistinguishable against the background. Another anomaly can be seen around 5 K, which is near the onset of the decrease of $\chi_{\perp}$ and could be related to it.

The discussed above behaviour is in many ways similar to the isostructural $Fe_{32+\delta}Ge_{33}As_2$ and $Fe_{32+\delta}Ge_{35-x}P_x$ compounds, which experience antiferromagnetic ordering, albeit at slightly lower temperatures (near 125 K), with similarly low Weiss temperatures slightly below −400 K.[19-21] Neutron diffraction and ^{57}Fe Mössbauer spectroscopy experiments showed that these compounds also experience reorientation of Fe magnetic moments, specifically at the Fe2 site.[21] The magnetic moments of Fe2 lie in the *ab* plane at higher temperatures and switch to the *c* direction at lower temperatures, while the rest of the Fe magnetic moments either remain parallel to the *c* axis or slightly deviate from it. Spin reorientation for $Fe_{32+\delta}Ge_{33}As_2$ occurred close to T_N with T_{SR} around 110 K,[19-21] while $Fe_{32+\delta}Ge_{35-x}P_x$ showed gradual spin reorientation in a span of 30 K between 20 and 50 K.[21] Mössbauer spectroscopy data also suggest that magnetic moments in $Fe_{32+\delta}Ge_{33}As_2$ deviate slightly from the *c* axis at low temperatures around 50 K, which also coincides with the increase in magnetic susceptibility.[19,21] In the case of $Fe_{32+\delta}Ge_{35-x}Si_x$, this deviation seems to occur at much lower temperatures and leads to a slight decrease in the susceptibility. Since the magnetic measurements for $Fe_{32+\delta}Ge_{33}As_2$ and $Fe_{32+\delta}Ge_{35-x}P_x$ were performed on several disoriented single crystals,[19,21] we cannot straightforwardly compare the effect of spin reorientation on the magnetic response of the compounds. Nevertheless, the comparison with $Fe_{32+\delta}Ge_{35-x}Si_x$ still provides some additional insights. While the averaged $\chi(T)$ curves for

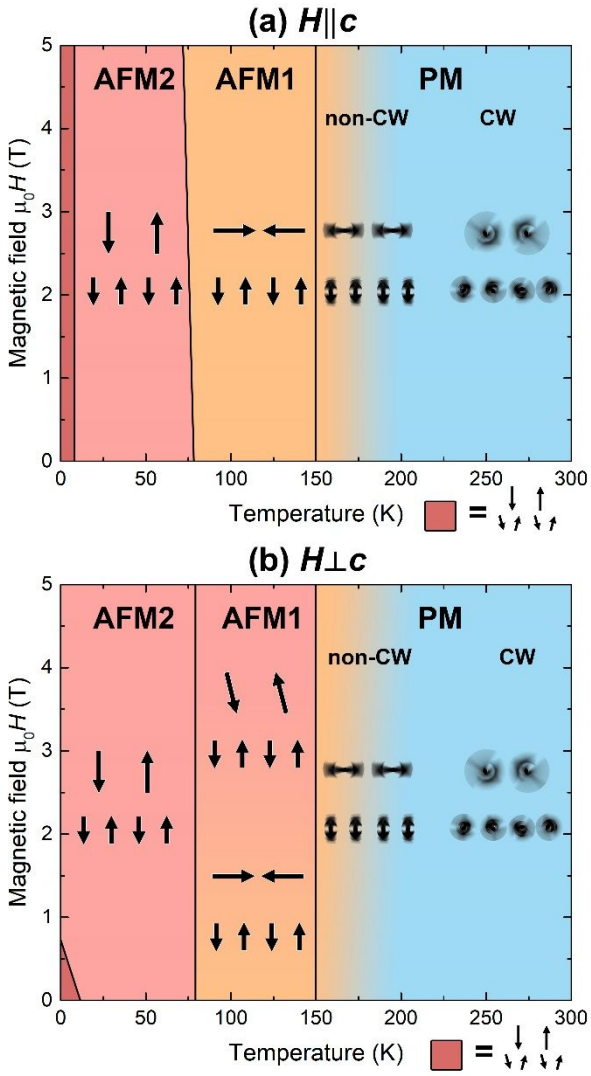

Fig. 13 Proposed magnetic phase diagrams of $Fe_{32+\delta}Ge_{35-x}Si_x$ for different directions of magnetic fields: parallel to the *c* axis (a) and perpendicular to it (b). PM stands for paramagnetic; CW stands for Curie-Weiss. Antiferromagnetic phases with different structures are marked as AFM1 and AFM2.

$Fe_{32+\delta}Ge_{35-x}Si_x$ measured in different field converge after the spin reorientation, this did not occur for $Fe_{32+\delta}Ge_{33}As_2$, as the significant field dependence of the susceptibility is conserved even below T_{SR} for the latter.[19] This field dependence shows that the magnetic structure of $Fe_{32+\delta}Ge_{33}As_2$ is still perturbed by the magnetic field even below T_{SR}, which is not the case for $Fe_{32+\delta}Ge_{35-x}Si_x$, where the magnetic moments are fully locked until at least 5 T. The field dependence of susceptibility below T_{SR} in the case of $Fe_{32+\delta}Ge_{33}As_2$ could be due to either magnetic moments of Fe1, Fe2, and Fe3 atoms being influenced by the in-plane oriented field or the Fe2 moments gradually reverting back to the *ab* plane in the magnetic fields oriented in the *c* direction.

Given that $Fe_{32+\delta}Ge_{33}As_2$, $Fe_{32+\delta}Ge_{35-x}P_x$, and $Fe_{32+\delta}Ge_{35-x}Si_x$ share the same underlying structure, one might expect this kind of similarity in their magnetic behaviour. However, it is not uncommon for related intermetallic systems to drastically alter their magnetic behaviour upon *p*-element doping, which could change not only superexchange interactions, but also direct exchange interactions between transition metal atoms if the changes in the interatomic distances are noticeable. For example, Ga doping of $MgFe_6Ge_6$-type RMn_6Ge_6 (R = Y, Sc, Lu) phases caused antiferromagnetic to ferromagnetic transition.[74,75] Structurally related $Fe_{23}Ge_{14-x}Al_{7+x}$ solid solution also displays antiferromagnetic to ferromagnetic transition upon increasing the Al concentration.[76,77] Si substitution for Ge in cubic FeGe transforms the metallic helimagnetic phase to a weakly magnetic semiconductor.[78,79] In $YMn_{1-x}Ga_{12-x}Ge_x$, the Ge substitution at first causes Curie temperature to increase and then gradually suppresses magnetic ordering.[80] In the case of the previously mentioned $FeGe_{1-x}Sb_x$ compounds, spin reorientation only develops in the moderate doping range (x = 0.1-0.12).[70-72]

The origin of the robustness of the $Fe_{32+\delta}Ge_{35-x}E_x$ magnetic behaviour might come from the topology of the Fe network and the placement of the E atoms. The Si and P atoms are found inside previously mentioned Fe cages forming Fe-rich layers, where direct Fe-Fe interactions seem to dominate. Neutron diffraction study showed that magnetic ordering in the Fe-rich layers for E = P and As is predominantly ferromagnetic.[21] Although the As_2 dumbbells are found between Fe-rich layers, the individual As atoms do not directly link Fe atoms from different Fe layers.

Based on the discussed above similarities in the $Fe_{32+\delta}Ge_{35-x}E_x$ crystal structure and magnetic behaviour, we assume that $Fe_{32+\delta}Ge_{35-x}Si_x$ is likely to share the key features of the magnetic structure of $Fe_{32+\delta}Ge_{33}As_2$ and $Fe_{32+\delta}Ge_{35-x}P_x$, including layered antiferromagnetic structure, with iron-rich layers consisting of Fe1, Fe3, Fe4, and Fe5 atoms ordering antiferromagnetically with respect to each other. Since the Fe2 atoms were shown to exhibit spin reorientation in $Fe_{32+\delta}Ge_{33}As_2$ and $Fe_{32+\delta}Ge_{35-x}P_x$,[21] we expect the Fe2 atoms in $Fe_{32+\delta}Ge_{35-x}Si_x$ to experience spin reorientation at T_{SR}, too. Given that the Fe2 atoms are isolated from the rest of the Fe sites, we also expect the rest of the Fe moments to retain their configuration in a manner similar to that of $Fe_{32+\delta}Ge_{33}As_2$ and $Fe_{32+\delta}Ge_{35-x}P_x$. Based on this picture, we can summarise the magnetic behaviour of $Fe_{32+\delta}Ge_{35-x}Si_x$ in the proposed magnetic phase diagram (Fig. 13).

Conclusions

Using both chemical transport and solid-state reactions, $Fe_{32+\delta}Ge_{35-x}Si_x$, a third member of the $Fe_{32+\delta}Ge_{35-x}E_x$ (E = *p*-element) family of compounds, have been isolated. Although $Fe_{32+\delta}Ge_{35-x}Si_x$ shares the same underlying two-dimensional intergrowth structure of the $MgFe_6Ge_6$ and Co_2Al_5 structure types with the P- and As-based members of the family, there are some notable features in its crystal structure that distinguish it from the other two phases, which stems from differences in electron configuration of Ge, As, Si, and P. The magnetic measurements of $Fe_{32+\delta}Ge_{35-x}Si_x$ reveal a rich magnetic behaviour with a rare combination of strong magnetic anisotropy, magnetic frustration and a spin reorientation, which arise from the complex topology of Fe and *p*-element networks.

The peculiar field dependence of the spin reorientation in $Fe_{32+\delta}Ge_{35-x}Si_x$, where the spins can be gradually rotated towards the *c* axis above T_{SR} by an applied magnetic field, but remain practically locked along this axis below T_{SR} even in strong fields, makes it particularly interesting to evaluate $Fe_{32+\delta}Ge_{35-x}Si_x$ as an antiferromagnetic memory material.

The example of $Fe_{32+\delta}Ge_{35-x}Si_x$ shows that the specific magnetic characteristics, such as temperatures of the magnetic transitions or the magnetic field response, can be tuned by chemical substitution without losing the main features of the $Fe_{32+\delta}Ge_{35-x}E_x$ magnetic behaviour. The large number of transition metal and *p*-element sites with different atomic environment presents a strong case to explore further tunability of the magnetic properties.

The discussed features of the $Fe_{32+\delta}Ge_{35-x}Si_x$ magnetic behaviour also demonstrate that even such a heavy modification of the kagome lattice can still preserve magnetic frustration, while the expected metallic behaviour of this phase makes it compelling to determine if the reciprocal space features of the kagome lattice can also be preserved in $Fe_{32+\delta}Ge_{35-x}Si_x$. Thus, the electronic structure and electronic transport of $Fe_{32+\delta}Ge_{35-x}Si_x$ await thorough experimental investigation.

Conflicts of interest

There are no conflicts to declare.

Data availability

The data supporting this article have been included as part of the Electronic Supplementary Information (ESI†). Crystallographic data for $Fe_{32+\delta}Ge_{35-x}Si_x$ has been deposited at the CCDC, accession codes: 2431926–2431930.

Author contributions

R.A.Kh.: Conceptualization, Methodology, Investigation, Visualization, Validation, Formal analysis, Data Curation, Writing – Original Draft, Writing – Review & Editing, Funding acquisition; V.Yu.V.: Investigation, Validation; A.V.M.: Investigation, Validation; A.N.S.: Investigation; A.V.B.: Investigation, Validation; A.N.K.: Investigation; A.O.P.: Investigation; Z.W.: Investigation, Validation, Writing – Review & Editing; E.V.D.: Writing – Review & Editing, Funding acquisition; R.S.: Validation, Writing – Review & Editing, Funding acquisition; A.V.Sh.: Conceptualization, Writing – Review & Editing, Supervision

Acknowledgements

This work has been supported by the Russian Science Foundation, grant # 24-73-00024. Z.W. and E.V.D. thank U. S. National Science Foundation for supporting the crystal structure study under grant # CHE-2400091. Work in Tallinn was supported by the European Regional Development Fund (Awards TK133 and TK134) and the Estonian Research Council (Projects Nos. PRG4 and PRG1702), and was cofunded by the European Union and Ministry of Education and Research via Project No. TEM-TA25. The authors also acknowledge the European Synchrotron Radiation Facility for granting the beam time and thank Dr. Wilson Mogodi for his help during the high-resolution PXRD experiments.

Notes and references

1 I. Syôzi, *Prog. Theor. Phys.* 1951, **6**, 306-308.
2 Q. Wang, H. Lei, Y. Qi and C. Felser, *Acc. Mater. Res.* 2024, **5**, 786-796.
3 J. X. Yin, B. Lian and M. Z. Hasan, *Nature* 2022, **612**, 647-657.
4 J. R. Chamorro, T. M. McQueen and T. T. Tran, *Chem. Rev.* 2020, **121**, 2898-2934.
5 Q. Du, M. G. Han, Y. Liu, W. Ren, Y. Zhu and C. Petrovic, *Adv. Quantum Technol.* 2020, **3**, Art. 2000058.
6 T. H. Han, J. S. Helton, S. Chu, D. G. Nocera, J. A. Rodriguez-Rivera, C. Broholm and Y. S. Lee, *Nature* 2012, **492**, 406-410.
7 H. Li, B. Ding, J. Chen, Z. Li, Z. Hou, E Liu, H. Zhang, X. Xi, G. W and W. Wang, *Appl. Phys. Lett.* 2019, **114**, Art. 192408.
8 D. Khadka, T. R. Thapaliya, S. Hurtado Parra, J. Wen, R. Need, J. M. Kikkawa and S. X. Huang, *Phys. Rev. Mater.* 2020, **4**, Art. 084203.
9 M. Kanagaraj, J. Ning and L. He, *Rev. Phys.* 2022, **8**, Art. 100072.
10 T. Chen, T. Tomita, S. Minami, M. Fu, T. Koretsune, M. Kitatani, I. Muhammad, D. Nishio-Hamane, R. Ishii, F. Ishii, R. Arita and S. Nakatsuji, *Nat. Commun.* 2021, **12**, Art. 572.
11 C. Mielke III, D. Das, J. X. Yin, H. Liu, R. Gupta, Y. X. Jiang, M. Medarde, X. Wu, C. Lei, J. Chang, P. Dai, Q. Si, H. Miao, R. Thomale, T. Neupert, Y. Shi, R. Khasanov, M. Z. Hasan, H. Luetkens and Z. Guguchia, *Nature* 2022, **602**, 245-250.
12 M. O. Ogunbunmi, H. S. Nair and A. M. Strydom, *Crit. Rev. Solid State Mater. Sci.* 2023, **48**, 480-501.
13 A. Bolens and N. Nagaosa, *Phys. Rev. B* 2019, **99**, Art. 165141.
14 Y. Okamoto, M. Nohara, H. Aruga-Katori and H. Takagi, *Phys. Rev. Lett.* 2007, **99**, Art. 137207.
15 N. Rogado, G. Lawes, D. A. Huse, A. P. Ramirez and R. J. Cava, *Solid State Comm.* 2002, **124**, 229-233.
16 M. M. Markina, P. S. Berdonosov, T. M. Vasilchikova, K. V. Zakharov, A. F. Murtazoev, V. A. Dolgikh, A. V. Moskin, V. N. Glazkov, A. I. Smirnov and A. N. Vasiliev, *Mater. Chem. Phys.* 2024, **319**, Art. 129348.
17 V. K. Singh, J. Link, K. Kargeti, S. K. Panda, I. Heinmaa, C. Dhanasekhar, M. Jawale, K.T. Kim, K.H. Kim, T. Chakrabarty, A. Mahajan, R. Stern and B. Koteswararao, *Phys. Rev. B*, 2024, **110**, 125112.
18 B. R. Ortiz, H. Zhang, K. Górnicka, D. S. Parker, G. D. Samolyuk, F. Yang, H. Miao, Q. Lu, R. G. Moore, A.F. May and M. A. McGuire, *Chem. Mater.* 2024, **36**, 8002-8014.
19 R. A. Khalaniya, A. V. Mironov, V. Y. Verchenko, A. Jesche, A. A. Tsirlin and A. V. Shevelkov, *Inorg. Chem.* 2016, **55**, 12953-12961.
20 R. A. Khalaniya, V. Y. Verchenko, Z. Wei, E.V. Dikarev, I. Heinmaa, R. Stern, A. Jesche, A.A. Tsirlin and A.V. Shevelkov, *J. Alloys Compd.* 2019, **779**, 229-236.
21 R. A. Khalaniya, A. V. Sobolev, V. Y. Verchenko, A. A. Tsirlin, A. Senyshyn, F. Damay, I. A. Presniakov and A.V. Shevelkov, *Dalton Trans.*, 2021, **50**, 2210-2220.
22 W. Buchholz and H. U. Schuster, *Z. Naturforschung B* 1978, **33** 877–880.
23 U. Burkhardt, M. Ellner, Y. Grin and B. Baumgartner, *Powder Diffr.* 1998, **13**, 159–162.

24 A. M. Mills and A. Mar, *J. Alloys Compd.* 2000, **298**, 82-92.
25 V. Petricek, M. Dusek and L. Palatinus, *Z. für Kristallogr. – Cryst. Mater*. 2014, **229**, 345–352.
26 K. Momma, T. Ikeda, A.A. Belik and F. Izumi. *Powder Diffr.* 2013, **28**, 184–193
27 K. Momma and F. Izumi, *J. Appl. Crystallogr.* 2011, **44**, 1272-1276.
28 C. Dejoie, M. Coduri, S. Petitdemange, C. Giacobbe, E. Covacci, O. Grimaldi, P. O. Autran, M. W. Mogodi, J. D. Šišak and A.N. Fitch, *J. Appl. Cryst.* 2018, **51**, 1721–1733.
29 V. Petříček, M. Dušek and L. Palatinus, Jana2000. Structure determination software programs. Institute of Physics: Praha, Czech Republic. 2000.
30 Yu. Grin, *In Modern Perspectives in Inorganic Crystal Chemistry*; E. Parthe, Ed.; Kluwer Academic Publishers: Norwell, MA, 1992; 77–95.
31 R. R. Olenych, L. G. Aksel'rud and Ya. P. Yarmolyuk, *Dopov. Akad. Nauk. Ukr.RSR, Ser A.,* 1981, **43**, 87–91.
32 V. Y. Verchenko, Z. Wei, A. A. Tsirlin, C. Callaert, A. Jesche, J. Hadermann, E. V. Dikarev and A. V. Shevelkov, *Chem. Mater.* 2017, **29**, 9954-9963.
33 K. Kanematsu and T. Ohoyama, *J. Phys. Soc. Jpn.* 1965, **20**, 236−242.
34 B. Lebech, J. Bernhard and T. Freltoft, *J. Phys.: Condens. Matter* 1989, **1**, 6105.
35 G. P. Felcher and J. D. Jorgensen, *J. Phys. C: Solid State Phys*. 1983, 16, 6281.
36 B. Malaman, J. Steinmetz and B. Roques, *J. Less-Common Met.* 1980, **75**, 155−176.
37 E. E. Havinga, H. Damsma and P. Hokkeling, *J. Less-Common Met.* 1972, **27**, 169−186.
38 R.A. Khalaniya, V.Y. Verchenko, A.V. Sobolev, I.A. Presniakov, Z. Wei, E.V. Dikarev and A.V. Shevelkov, *J. Alloys Compd.* 2022, **902**, 163759.
39 M. Schütte, R. Wartchow and M. Binnewies, *Z. Anorg. Allg. Chem.* 2003, **629**, 1846-1850.
40 P. Lecocq and A. Michel, *Bull. Soc. Chim. Fr*. 1965, 307-310.
41 R. Wartchow, S. Gerighausen and M. Binnewies, *Z. Kristallogr. - New Cryst. Struct.* 1997, **212**, 320-320.
42 Y. Dusausoy, J. Protas, R. Wandji and B. Roques, *Acta Crystallogr., Sect. B*, 1971, **27**, 1209-1218.
43 B. Aronsson, D. H. Templeton, S. Rundqvist, E. Varde and G. Westin, *Acta Chem. Scand.*, 1960, **14**, 1414-1418.
44 A. V. Tkachuk and A. Mar, *Acta Crystallogr., Sect. E: Struct. Rep. Online* 2005, **61**, i1−i2.
45 J.Yan, S. Wu, X. Ou, L. Zeng and J. Hao, *Powder Diffr.* 1998, **13**, 241−243.
46 A. Earnshaw, N. Greenwood. Chemistry of the Elements (2 ed.); Butterworth-Heinemann: Oxford, 1997.
47 Additional crystallographic information files for ref. 20 not included in the original publication: CSD 2431312-2431314, 2431316
48 R. A. Khalaniya, V. Y. Verchenko, E. M. Zonov, R. Stern and A. V. Shevelkov, *Inorg. Chem.*, 2024 **63**, 21099-21109.
49 A. N. Bogdanov, A. V. Zhuravlev and U. K. Rößler, *Phys. Rev. B: Condens. Matter Mater. Phys.* 2007, **75**, Art. 094425.
50 Z. V. Pchelkina, V. V. Mazurenko, O. S.Volkova, E. B. Deeva, I. V. Morozov, V. V. Shutov, S. I. Troyanov, J. Werner, C. Koo, R. Klingeler and A. N. Vasiliev, *Phys. Rev. B* 2018, **97**, Art. 144420.
51 A. A. Vorobyova, A. I. Shilov, F. M. Spiridonov, A. V. Knotko, I. L. Danilovich, A. N. Vasiliev and I. V. Morozov, *Russ. Chem. Bull.* 2020, **69**, 704-711.
52 A. Vorobyova, I. Danilovich, I. Morozov, Y. Ovchenkov, A. Vasiliev, O. Volkova, A. Iqbal, B. Rahaman and T. Saha-Dasgupta, *J. Alloys Compd.* 2022, **929**, Art. 167197.
53 R.A. Khalaniya and A.V. Shevelkov, *J. Solid State Chem.*, 2019, **270**, 118–128.
54 O. Zaharko, P. Schobinger-Papamantellos, C. Ritter, J. Rodŕiguez-Carvajal and K.H.J. Buschow, *J. Magn. Magn. Mater.* 1998, **187**, 293–308.
55 R. Nishihara, M. Akimitsu, T. Hori, H. Niida, K. Ohoyama, M. Ohashi, Y. Yamaguchi and Y. Nakagawa, *J. Magn. Magn. Mater.*, 1999, **196–197**, 665–666.
56 T. Mazet, O. Isnard and B. Malaman, *Solid State Commun.*, 2000, **114**, 91–96.
57 T. Mazet and B. Malaman, *J. Phys.: Condens. Matter.*, 2000, **12**, 1085–1095.
58 M.A. Avila, T. Takabatake, Y. Takahashi, S.L. Bud'ko and P.C. Canfield, *J. Phys. Conden. Matter*, 2005, **17**, 6969–6979.
59 T. Mazet, V. Ban, R. Sibille, S. Capelli and B. Malaman, *Solid State Commun.*, 2013, **159**, 79–83.
60 N. Plugaru, C. Piquer, F. Grandjean, J. Rubín and J. Bartolomé *AIP Conf. Proc.* 2005. 765(1) 239–244.
61 O. Zaharko, P. Schobinger-Papamantellos, J. Rodŕiguez-Carvajal and K. H. J. Buschow. *J. Alloys Compd.* 1999, **288**, 50–56.
62 T. Hori, H. Shiraishi, H. Kato, G. Kido and Y. Nakagawa, *J. Magn. Magn. Mater.* 1992, **104**, 2043–2044.
63 J. M. Cadogan and D. H. Ryan, *J. Alloys Compd.* 2001, **326**, 166–173.
64 J. M. Cadogan, D. H. Ryan and J. D. Cashion *J. Phys.: Condens. Matter.* 2007, **19**, Art. 216204.
65 T. Mazet and B. Malaman *J. Alloys Compd.* 2001, **325**, 67–72.
66 J. B. Forsyth, C. Wilkinson and P. Gardner, J. Phys. F: Met. Phys., 1978, 8, 2195–2202.
67 J. Bernhard, B. Lebech and O. Beckman, J. Phys. F: Met. Phys., 1984, 14, 2379–2393.
68 L. Häggström, T. Ericsson, R. Wäppling and E. Karlsson, *Phys. Scr.*, 1975, **11**, 55–59.
69 X. Teng, J. S. Oh, H. Tan, L. Chen, J. Huang, B. Gao, J.-X. Yin, J.-H. Chu, M. Hashimoto, D. Lu, C. Jozwiak, A. Bostwick, E. Rotenberg, G.E. Granroth, B. Yan, R. J. Birgeneau, P. Dai and M. Yi, *Nat. Phys.*, 2023, **19**, 814-822.
70 Q. D. Gibson, R. Daou, M. Zanella, J. Alaria and M. J. Rosseinsky, *Phys. Rev. B* 2023 **108**, Art. 035102.
71 J. Huang, C. Shang, J. Qin, F. Pan, B. Shi, J. Wang, J. Liu, D. Xu, H. Zhang, H. Wang, L. Hao, W. Bao and P. Cheng, *Phys. Rev. B*, 2023 **108**, Art. 184431.
72 Z. Lin, C. Shi, X. Xu, Q. Liu, J. Y. Liu, W. Yang, J. Yang, B. Kang, S. Cao and J. K. Bao, *J.Solid State Chem.* 2025, **345**, Art. 125243.
73 K. Kanematsu, *J. Phys. Soc. Jpn.* 1965, **20**, 36–43.
74 G. Venturini, *J. Alloys Compd*. 2000, **309**, 20–25.
75 G. Venturini, *J. Alloys Compd*. 2000. **311**, 101–108.
76 G. R. Reisinger, H.S. Effenberger and K.W. Richter, *J. Alloys Compd*. 2017, **693**, 692–699.
77 J. Kitagawa, G. Yakabe, A. Nakayama, T. Nishizaki and M. Tsubota, *J. Solid State Chem*. 2020, **284**, Art. 121188.
78 H. Wilhelm, M. Baenitz, M. Schmidt, U. K. Rößler, A. A. Leonov and A. N. Bogdanov, *Phys. Rev. Lett.*, 2011, **107**, 127203.
79 S. Yeo, S. Nakatsuji, A. D. Bianchi, P. Schlottmann, Z. Fisk, L. Balicas, P. A. Stampe and R. J. Kennedy, *Phys. Rev. Lett.* 2003, **91**, Art. 046401.
80 M. C. Francisco, C. D. Malliakas, P. M. B. Piccoli, M.J. Gutmann, A. J. Schultz and M. G. Kanatzidis, *J. Am. Chem. Soc*. 2010, **132**, 8998–9006.

Data availability:

- The data supporting this article have been included as part of the Electronic Supplementary Information (ESI†).
- Crystallographic data for $Fe_{32+\delta}Ge_{35-x}Si_x$ has been deposited at the CCDC, accession codes: 2431926–2431930.